

HERMES spectroscopy of normal A and Am stars

Otto Trust¹^{*}, Edward Jurua¹[†], Peter De Cat², Santosh Joshi³, and Patricia Lampens²

¹*Department of Physics, Mbarara University of Science and Technology, P.O. Box 1410, Mbarara, Uganda*

²*Royal Observatory of Belgium, Ringlaan 3, B-1180 Brussels, Belgium*

³*Aryabhata Research Institute of Observational Sciences, Manora Peak, Nainital- 263002, India*

Accepted XXX. Received YYY; in original form ZZZ

ABSTRACT

The nominal *Kepler* mission provided very high-precision photometric data. Using these data, interesting phenomena such as spots, and “hump and spike” features were observed in the light curves of some normal A and metallic lined A stars (Am stars). However, the connection between such phenomena and the chemical peculiarity of the Am stars is still unclear. In order to make progress on these issues, it is important to collect high-resolution spectroscopic data to determine their fundamental parameters and individual chemical abundances. In this paper, we present a spectroscopic study of a sample of “hump and spike” stars in the nominal *Kepler* field. We used data collected with the High Efficiency and Resolution Mercator Échelle Spectrograph (HERMES). We determined the spectral type of these stars and obtained the atmospheric stellar parameters such as effective temperatures, surface gravities, projected rotational, microturbulent and radial velocities. We also performed a detailed individual chemical abundance analysis for each target. We confirmed KIC 3459226 and KIC 6266219 as Am stars, KIC 9349245 as a marginal Am star, while KIC 4567097, KIC 4818496, KIC 5524045, KIC 5650229, KIC 7667560, and KIC 9272082 are non-Am stars. To estimate their evolutionary phases, all the stars were placed in the Hertzsprung-Russell (HR) diagram. Based on their spectral classification and chemical abundance pattern, we reclassified KIC 6266219 (previously treated as chemically normal) as an Am star (kA3hA7mF1) and KIC 9272082 (previously treated as Am) as non-Am.

Key words: stars: chemically peculiar – stars: rotation – stars: starspots – stars: general – techniques: spectroscopic

1 INTRODUCTION

Over the previous few decades, many space missions were launched, such as Microvariability and Oscillations of Stars (MOST; Rucinski et al. 2003), Convection, Rotation and planetary Transits (CoRoT; Baglin et al. 2006), *Kepler* (Borucki et al. 2010) and Transiting Exoplanet Survey Satellite (TESS; Ricker et al. 2014), which are mainly searching for exo-planets and enabling asteroseismology of pulsating stars. More projects like PLANetary Transits and Oscillations of stars (PLATO; Rauer et al. 2014) and Wide Field Infrared Survey Telescope (WFIRST; Gehrels et al. 2015) will be launched in the near future. To understand the characteristics of exo-planets, the stellar parameters of the host stars are relevant (Howard et al. 2013). For pulsating stars, especially those with solar-like oscillations, asteroseismology has played a big role in determining the stellar parameters using high-precision photometric data from space telescopes.

Even when high-precision photometric data are available, ground-based spectroscopy is still essential in determining complementary stellar parameters of most stars and it is still widely used (e.g; Santos et al. 2005; Sousa et al. 2015; Gandolfi et al. 2018; Kassounian et al. 2019; Eisner et al. 2020). For the intermediate mass main-sequence (MS) stars (A- and F-type), where chemically peculiar (CP) stars are common (about 10%), spectroscopy plays a big role in determining the individual chemical abundances in addition to the atmospheric stellar parameters (e.g; Fossati et al. 2008; Gebran & Monier 2008; Gebran et al. 2008, 2010).

The CP stars exhibit atmospheric abundances which are significantly different from the solar values. Based on the magnetic field strength and strength of absorption lines in their optical spectra, Preston (1974) categorised the CP stars into four major groups: CP1 stars (the metallic-line or Am/Fm stars), CP2 stars (the magnetic Ap stars), CP3 stars (the Mercury-Manganese or HgMn stars) and CP4 stars (the He-weak stars). The CP1 (Am) are the most numerous CP stars followed by CP2 (Ap) stars in the intermediate mass MS part of the Hertzsprung-Russell (HR) di-

* E-mail: otrust@must.ac.ug

† E-mail: ejurua@must.ac.ug

agram. The Am stars are characterized by under-abundance of certain light elements (such as Ca and Sc) and excess of metals, in addition to the very weak or non-detectable magnetic fields in general (Conti 1970; Preston 1974; Romanyuk 2007). This implies that for Am stars, three spectral classifications are always given: (i) based on the Balmer lines, which give good estimates of effective temperature (T_{eff}), (ii) based on the Ca II K-line ($\lambda\lambda$ 393.4 nm) which gives an earlier spectral type since it is weaker than for normal stars and (iii) based on the metallic lines which give a later spectral type because they are enhanced relative to normal stars. Am stars whose spectral types are derived from the Ca II K-line and metallic lines differ by 5 or more subtypes are called classical Am stars. For marginal Am stars, this difference is less than 5 subtypes. The CP2 stars are known for large excesses (up to several orders of magnitude) of heavy elements such as Si, Hg or the rare-earth elements Sr, Cr, Eu, Nd, Pr etc (Conti 1970; Preston 1974; Kurtz & Martinez 2000; Romanyuk 2007). The CP2 stars are also characterized by the presence of well organized magnetic fields with strengths of up to several tens of kG (Aurière et al. 2007), which could be of fossil origin (Braithwaite & Spruit 2004). The CP3 stars possess enhanced Hg II ($\lambda\lambda$ 398.4 nm) and/or Mn II lines and weak lines of light elements (such as He, Al and N) in their spectra. The majority of CP3 stars are very slow rotators with $v \sin i \leq 20 \text{ km s}^{-1}$ and are also characterised by weak or non-detectable magnetic fields (Preston 1974; Smith 1997; Bohlender et al. 1998). The CP4 stars are characterised by anomalously weak He I lines in their spectra. They are also slow rotators with magnetic field strengths of upto the orders of 1 kG (Jones & Wolff 1974; Preston 1974).

The chemical peculiarities in CP stars are thought to mainly originate from the interplay between radiative levitation and gravitational settling, a process known as atomic diffusion (Michaud 1970; Watson 1970; Khokhlova 1981; Hui-Bon-Hoa 2000; Richer et al. 2000; Turcotte 2003; Théado et al. 2011). Based on this theory, in the absence of mixing, light elements drift under the influence of gravity and are seen as under-abundant while heavy elements are radiatively driven outward (reflected as overabundant). This theory requires calm and stable atmospheres which are facilitated by the slow rotation of CP stars (Takeda et al. 2008; Fossati et al. 2008; Stateva et al. 2009; Abt 2009) and by strong magnetic fields in the case of Ap stars. In addition to turbulent mixing, another actor in the process could be weak mass loss (Richer et al. 2000; Richard et al. 2001; Michaud et al. 2004; Talon et al. 2006). It has also been reported to reduce the main surface chemical abundance anomalies, in models including atomic diffusion, to the observed levels in CP stars (Michaud et al. 1983; Michaud & Charland 1986; Alecian 1996; Vick et al. 2010, 2011). The strong magnetic fields are thought to stabilise the convective material, while slow rotation minimises meridional circulation and in-turn minimises mixing that would counteract atomic diffusion. Rotation plays a big role in constraining the physics of CP stars such as pulsations (Dziembowski et al. 1988; Soufi et al. 1998), overshooting (Browning et al. 2004; Costa et al. 2019) and the observed chemical abundances (Turcotte 2002; Murphy 2014).

Given the high-precision and almost continuous photometric data from space missions like the nominal *Kepler* mission, K2 (Howell et al. 2014) and TESS, the rotation

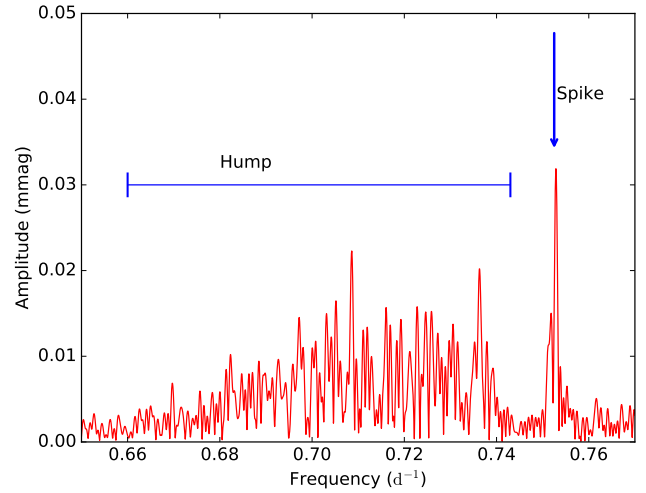


Figure 1. The “hump and spike” features in an amplitude spectrum for KIC 6192566 as reported by Trust et al. (2020).

of A-type (CP and normal) stars has been studied assuming spot induced rotational modulation (Kron 1947; Mosser et al. 2009; Balona 2013) and based on the “hump and spike” features in their frequency spectra (Saio et al. 2018; Trust et al. 2020). Briefly, the “hump and spike” stars were named by Saio et al. (2018). Their frequency spectra possess a sharp peak (“spike”) on the high frequency side of a broad hump of very close frequencies (“hump”) as shown in Fig. 1 by Trust et al. (2020). The broad humps are induced by Rossby waves (r modes) and the spikes are the rotation frequencies induced by one or more spots (Saio et al. 2018). The “hump and spike” stars are a test bed to study the association of the r modes with rotation and other processes (such as atomic diffusion) that affect their chemical peculiarity. The period of stellar rotation can also be determined using seismic splitting (Saio 1981; Claverie et al. 1981) and chromospheric activity, especially Ca II emission (Noyes et al. 1984). However, we obtain a complete rotational profile when the projected rotational velocity ($v \sin i$) is known too. The $v \sin i$ can be spectroscopically retrieved from the broadening of the absorption lines (Kaler 1989).

To search and study the pulsational variabilities in Ap and Am/Fm stars, a dedicated ground-based project, the Nainital-Cape survey, was initiated between astronomers of India and South Africa. With time, astronomers from other countries joined this programme making it a multi-national collaborative project and a number of results have been published (e.g; Ashoka et al. 2000; Martinez et al. 2001; Joshi et al. 2003, 2006, 2009, 2010, 2012, 2016, 2017). The success of the Nainital-Cape survey and the discovery of “hump and spike” features in the frequency spectra (Balona 2013; Balona et al. 2015; Saio et al. 2018) of a number of normal A and Am stars motivated us to initiate a collaboration with astronomers from India, Uganda and Belgium, to study the phenomena responsible for the observed chemical peculiarities in Am stars. The first results are presented in Trust et al. (2020). This paper is the second of the series whose objective is to characterize the “hump and spike” stars. This involves the spectral classification, determination of atmospheric stel-

lar parameters and individual chemical abundances of our targets.

This paper is organised as follows. The data are discussed in Sect. 2. Spectral classification is presented in Sect. 3, while atmospheric parameters and individual chemical abundance analyses are given in Sect. 4. The comments on individual stars and their location in the HR diagram are discussed in Sects. 5 and 6, respectively, while the conclusion is given in Sect. 7.

2 THE DATA

2.1 Selection criteria

The majority of stars in this study are part of the samples analysed by Trust et al. (2020). These are normal A and Am stars with “hump and spike” features in their frequency spectra which were selected from Balona (2013), Balona et al. (2015), and Gray et al. (2016). Of the 171 “hump and spike” stars studied by Trust et al. (2020), we selected those with the $V \leq 10.5$ mag and not reported in the literature as members of binary systems. Stars with $V \leq 10.5$ mag are bright enough to obtain high-quality HERMES spectra with SNR of at least 100 per pixel in a maximum exposure time of one hour. In this paper, we present a spectroscopic analysis for 9 such stars.

2.2 Observations and Data Reduction

The high-resolution spectroscopic observations were made on the nights of 02, 06 and 07 November 2018, using the HERMES (Raskin et al. 2011) spectrograph mounted at the Cassegrain focus of the 1.2-m Mercator telescope located at La Palma, Spain. In a single exposure, this spectrograph records optical spectra in the wavelength (λ) range 377 to 900 nm across the 55 spectral orders. The resolving power of this instrument in the high-resolution mode is 85 000 with radial velocity stability of about 50 m s^{-1} , and excellent throughput (Raskin et al. 2011). The log of the observations collected with HERMES is presented in Table 1.

The spectra were reduced using a dedicated HERMES pipeline. The usual reduction procedure for échelle spectra was applied. The steps include subtraction of the bias and stray light, flat-field correction, order-by-order extraction, wavelength calibration with Thorium-Argon lamps, cosmic rays removal and merging of the orders (Raskin et al. 2011). The procedure also provides the SNR, which in our case, falls in the range 30–110 (at $\lambda = 500, 650$ and 810 nm) on average and are listed in Table 1. Normalisation of all the spectra to the local continuum was performed manually using the *continuum* task of the IRAF package¹. Finally, all the spectra were systematically corrected for barycentric motion.

For some of the stars, we collected more than one spectrum (Table 1). For these stars, all the spectra were median-combined and we performed investigations on the average spectrum. The SNR of the median spectra lies in the range of 110–220 on average.

¹ <http://iraf.noao.edu/>

3 SPECTRAL CLASSIFICATION

Prior to the determination of atmospheric parameters and chemical abundances, we performed a spectral classification analysis of the targets on the MK classification system (Morgan et al. 1943; Gray & Corbally 2009). Spectral classification provides essential details about a star’s chemical peculiarity and initial atmospheric parameters (Gray & Corbally 2009). The spectral type and luminosity class are based on the similarity between the observed spectra and those of well-known standards, taking into account essential hydrogen and metal lines. We classified the stars using two data types, (i) spectral energy distribution (SED) and (ii) HERMES spectra.

Using the VOSA package (Bayo et al. 2008) and least-squares minimisation technique, we cross-matched the SED (discussed in Sect. 4.2) of the targets with the template libraries built by Kesseli et al. (2017) from SDSS spectra. The resulting spectral types are indicated with “1a” in Table 2. The uncertainty in the spectral type is about 3 subtypes.

Classification of the HERMES spectra was performed using the code MKCLASS (Gray & Corbally 2014). Given that the observation time is always limited and not all the standards are always visible at the time of observation of the targets, we used the available standard libraries by Gray et al. (2003). For the observations of these standard libraries, they used the Dark Sky Observatory (DSO) 0.8-m telescope in Northwestern part of North Carolina in combination with the Gray/Miller classification spectrograph having two gratings with 600 and 1200 grooves mm^{-1} , respectively. The standards were observed in the violet-green spectral region at a resolution range of $0.15\text{--}0.36 \text{ nm} / 2 \text{ pixels}$ (Gray & Corbally 2014).

The spectra for the standards and our sample stars are not from the same spectrograph/grating combination. To approximate the specifications of the standards as close as possible, we truncated the wavelength range, re-binned and convolved the HERMES spectra with a Gaussian of appropriate full width at half maximum (FWHM) determined by the intended final resolution of $0.36 \text{ nm} / 2 \text{ pixels}$.

The metric-distance technique (LaSala 1994), which relies on a weighted least-square comparison of the spectra of the program star with those of the MK standard stars, was used (Gray & Corbally 2014). For each star, the spectral type was determined three times, each time based on different lines, that is; hydrogen lines (H γ and H σ lines), metal lines, and the Ca II K-line. For a normal star, all the three regions correspond to the same spectral type. However, in the case of the chemically peculiar stars, such as Am stars, the three regions give different spectral types (Gray & Corbally 2009). The obtained spectral types and luminosity classes are indicated with “1b” in Table 2. The spectral types and luminosity classes of the sample lie in the range B9 to F1 and III to V, respectively.

4 ATMOSPHERIC PARAMETERS AND CHEMICAL ABUNDANCES

Photometry and spectroscopy are the traditional methods used to determine atmospheric parameters. In the case of well-studied pulsating stars, asteroseismology has proved to

Table 1. The observation log for the target stars. The right ascension (α_{J2000}) and declination (δ_{J2000}) given by [Gaia Collaboration \(2018\)](#) and the V-band magnitude estimated by [Høg et al. \(2000a\)](#) are included.

KIC No.	Other Name	α_{J2000} (hh mm ss)	δ_{J2000} (dd mm ss)	V (mag)	BJD (2 450 000+) (day)	Number of Spectra	SNR (@ 500, 650 and 810 nm)	Total Exposure Duration (min)
3459226	BD +38°3705	19 40 50.1201	+38 32 27.0912	10.11	8 430	5	27–51	75.0
4567097	HD 184469	19 32 55.9360	+39 39 45.7237	7.75	8 429	1	90–111	10.0
4818496	HD 177592	19 03 39.2582	+39 54 39.2370	8.07	8 429	1	99–125	12.5
5524045	BD +40°3639	19 15 14.7706	+40 43 45.3009	9.36	8 429	2	42–71	40.0
5650229	HD 226697	19 56 36.7584	+40 48 32.0652	9.92	8 430	3	37–55	42.5
6266219	TYC3127-2016-1	18 56 58.4055	+41 36 45.3267	9.87	8 425	3	25–44	60.0
7667560	HD 177458	19 02 49.8015	+43 21 21.1749	9.63	8 425	3	23–51	60.0
9272082	HD 179458	19 10 33.7965	+45 45 03.9964	8.95	8 429	4	55–86	50.0
9349245	HD 185658	19 38 05.1898	+45 53 03.8221	8.11	8 430	1	70–104	10.0

give good results, especially since high-precision photometric data from space missions like CoRoT and *Kepler* became available. That does not alter the fact that spectroscopy has always remained robust and relevant in providing atmospheric parameters. However, a good initial guess is very essential to attain convergence during the process of atmospheric parameter determination based on spectral synthesis. Some of the methods from which the initial guesses can be obtained include photometric colour indices (Sect. 4.1) and SED fitting (Sect. 4.2).

4.1 Atmospheric parameters from photometry

We computed stellar parameters using the available photometric indices from photometric databases, namely, *ubv* β ([Hauck & Mermilliod 1998](#)), 2MASS ([Cutri et al. 2003](#); [Skrutskie et al. 2006](#)) and UBV ([Oja 1985](#)). All values were retrieved from the General Catalog of Photometric data² ([Mermilliod et al. 1997](#)). The reddening parameter $E(B-V)$ was computed from 3D models ([Green 2018](#); [Green et al. 2019](#)) using the GAIA parallaxes ([Gaia Collaboration 2018](#)) and the stellar galactic coordinates from the SIMBAD database³ ([Wenger et al. 2000](#)). The resulting values of $E(B-V)$ are reported in column 3 of Table 3.

In the General Catalog of Photometric data, the Strömgren β indices are available for KIC 9272082 and KIC 9349245 only. We calculated T_{eff} and $\log g$ from *ubv* β indices using a routine originally written by [Moon \(1985\)](#), based on [Moon & Dworetzky \(1985\)](#) and corrected by [Napiwotzki et al. \(1993\)](#). We determined the overall metallicity ($[M/H]$) using the Strömgren δm_o index for A-type (A0–F0) stars ([Smalley 1993](#)). We considered errors (systematic and statistical) of 200 K, 0.10 dex ([Napiwotzki et al. 1993](#)) and 0.13 dex ([Smalley 1993](#)) in T_{eff} , $\log g$ and $[M/H]$, respectively. The results based on Strömgren photometry are given in columns 4 to 6 of Table 3.

Finally, we computed T_{eff} from the 2MASS and UBV photometric systems. This is based on the strong correlation of T_{eff} with the $(V-K)_o$ ([Masana et al. 2006](#)) and $(B-V)_o$ indices ([Sekiguchi & Fukugita 2000](#)). Since T_{eff} is weakly

correlated with $\log g$ and $[M/H]$, we fixed $\log g = 4.0$ dex and $[M/H] = 0.0$ dex (solar metallicity). For each system, we estimated the uncertainties in T_{eff} based on the errors of the photometric indices, i.e. $E(B-V)$ (0.02 mag), $[M/H]$ (0.10 dex) and $\log g$ (0.10 dex) ([Kahraman Aliçavuş et al. 2016](#)). The photometric parameters and their uncertainties are listed in columns 7 and 8 of Table 3. The T_{eff} (2MASS) and T_{eff} (UBV) for KIC 4567097 and KIC 6266219 do not agree within 1σ . In addition, T_{eff} (*ubv* β) values for KIC 9272082 and KIC 9349245 seem to be about 500 K higher compared to the values of T_{eff} (2MASS) and T_{eff} (UBV). The difference in T_{eff} could be introduced by the assumption that $(V-K)$ and $(B-V)$ are completely $\log g$ and metallicity independent ([Ramírez & Meléndez 2005](#)). Some of the target stars in the sample are chemically peculiar and/or variable, which may introduce additional errors in the calibration process ([Herdin et al. 2016](#)).

4.2 Atmospheric Parameters from SED

We can measure stellar parameters from the SED of a star. SEDs are built using spectrophotometry obtained in different wavelengths, ideally from ultraviolet to infrared. For this purpose, we adopted the VOSA tool.

In the first step, the tool automatically searches for spectrophotometric observations in different databases, i.e. the Tycho II ([Høg et al. 2000b](#)), 2MASS ([Skrutskie et al. 2006](#)), WISE ([Wright et al. 2010](#)), and GAIA DR2 ([Maíz Apellániz & Weiler 2018](#)) catalogs, complemented with Johnson ([Johnson & Morgan 1953](#); [Oja 1985](#)), Strömgren ([Hauck & Mermilliod 1998](#)), Galaxy Evolution Explorer (GALEX; [Bianchi & GALEX Team 2000](#)), Sloan ([Brown et al. 2011](#)) and Pan-STARRS1 ([Chambers et al. 2016](#)) photometry, when available. We estimated the extinction (A_v) for each target using $A_v = R_v \times E(B-V) = 3.1 \times E(B-V)$ ([Brown et al. 2011](#)). We determined $E(B-V)$ as discussed in Sect. 4.1. Also the stellar distance is required to construct SEDs. We used distances calculated from the GAIA parallaxes ([Gaia Collaboration 2018](#)) that are listed in column 2 of Table 3. The SEDs for all the stars under study are shown in Fig. 2 as filled circles. Using ATLAS9 Kurucz ODFNEW/NOVER models ([Castelli et al. 1997](#)) in the VOSA tool, we performed a least-square fit to these SEDs to obtain T_{eff} , $\log g$ and $[M/H]$. The results are represented by

² <https://gcpd.physics.muni.cz>

³ <https://simbad.u-strasbg.fr/simbad/>

Table 2. The spectral classification of the target stars.

KIC	Sp type	Comment	References	
3459226	F2 Dwarf		1a	
	kA2hF0mF3		1b	
	kA2hF0mF2		2	
4567097	A0 Giant		1a	
	B9 III	vgood	1b	
	B9		3	
4818496	A1 Dwarf		1a	
	A1 V	good	1b	
	A0		3	
5524045	A1 Dwarf		1a	
	A6 mA0 V metal-weak	good	1b	
	A3 mA0 IV metal-weak		2	
	A1V		4	
	A0.5Va+		5	
5650229	A1 Dwarf		1a	
	A8 mA0 V metal-weak		1b	
	A3 mA1 IV metal-weak		2	
	A0 IV-V		2	
	A2		3	
6266219	F1 Dwarf		1a	
	kA3hA7mF1		1b	
	7667560	A9 Dwarf		1a
		A6 mA0 V metal-weak	good	1b
		A		3
9272082	A9 Dwarf		1a	
	A4 V	good	1b	
	A5 IV-V		2	
	A0		3	
	A3 V		4	
	A7		6	
	Am		7	
	A5m		8	
9349245	F0 Dwarf		1a	
	A8 IV (Sr)	good	1b	
	A8 V (Sr)		2	
	A5		3	
	A7 III		4	
	Am		9	
F2 III		10		

References: (1) This study based on: (a) fitting SED with [Kesseli et al. \(2017\)](#) template libraries using the VOSA tool, and (b) HERMES spectra using MKCLASS ([Gray & Corbally 2014](#)); (2) [Gray et al. \(2016\)](#); (3) [Cannon & Pickering \(1993\)](#); (4) [Frasca et al. \(2016\)](#); (5) “a+” denotes higher luminosity main-sequence star ([Niemczura et al. 2015](#)); (6) [Floquet \(1970\)](#); (7) [Bertaud \(1960\)](#); (8) [Macrae \(1952\)](#); (9) [Catanzaro et al. \(2015\)](#); (10) [Niemczura et al. \(2017\)](#)

the blue lines in Fig. 2. The uncertainties calculated by the VOSA tool on these parameters are underestimated by a factor of about 2 because they only account for the internal errors on the SED-fitting procedure. This is attributed to the intrinsic limitations of the method ([Bayo et al. 2008](#); [McDonald et al. 2012](#); [Catanzaro et al. 2015](#)). Therefore, to have more realistic error limits, we doubled the uncertainties of the quantities (cf. [Catanzaro et al. 2015](#)), making the

$T_{\text{eff,SED}}$ uncertainties comparable to those from other photometric techniques. The results of the SED fitting procedure are listed in columns 9 to 12 of Table 3.

4.3 Atmospheric Parameters from Spectroscopy

In this section we evaluate the fundamental astrophysical quantities of our targets, i.e. T_{eff} , $\log g$, $v \sin i$, microturbulent velocity (ξ), and radial velocity (v_{rad}).

The first step is to determine v_{rad} by computing the cross correlation function (CCF) using different pre-selected masks built from line lists using the code iSPEC ([Blanco-Cuaresma et al. 2014](#); [Blanco-Cuaresma 2019](#)). We computed $v \sin i$ by comparing the observed spectra with a grid of synthetic spectra, pre-computed with plane-parallel ATLAS9⁴ model atmospheres ([Castelli & Kurucz 2003](#)) for different values of T_{eff} and of $\log g$, in the wavelength range 516–519 nm (Mg I triplet). This comparison was performed with a least-square method based on the MINUIT minimization package used by the GIRFIT package ([Frémat et al. 2006](#)).

For stars with $T_{\text{eff}} \geq 8000$ K, the Balmer lines become more sensitive to $\log g$ than to T_{eff} . For such targets (KIC 4567097, KIC 4818496, KIC 5524045, KIC 5650229, KIC 6266219, KIC 7667560, and KIC 9272082), we used GIRFIT to derive the temperature from the spectral region with a high number of metal lines (495–570 nm). The SNR of this spectral region was first improved using the least-square deconvolution (LSD) method described in [Tkachenko et al. \(2013\)](#). Using GIRFIT, we fitted 10–15 nm segments of the denoised spectrum and calculated the average T_{eff} for all the segments. For KIC 3459226 and KIC 9349245 ($T_{\text{eff}} < 8000$ K), we determined T_{eff} using hydrogen line profiles. The errors are a contribution of uncertainties encountered in continuum normalization and errors from the fitting procedure. We adopted an error of 100 K as a contribution from continuum normalization ([Catanzaro et al. 2015](#)).

The values of $\log g$ were estimated by two different methods depending on T_{eff} of each object. For target stars with $T_{\text{eff}} > 8000$ K, we computed $\log g$ from fitting hydrogen line wings. At $T_{\text{eff}} < 8000$ K the Balmer lines lose their sensitivity to $\log g$, and so metal lines (Fe I/Fe II and/or Mg I triplet) were used instead.

We uniquely obtained ξ by fitting iron lines using the MOOG radiative transfer code ([Snedden et al. 2012](#)), ATLAS9 model atmospheres, the Vienna Atomic Line Database (VALD) line-list ([Kupka et al. 1999](#)) and [Asplund et al. \(2009\)](#) solar abundances, all incorporated in an integrated software iSPEC. We determined the initial guess for ξ from the relation ([Gebran et al. 2014](#)),

$$\xi = 3.31 \times \exp \left[- \left(\log \left(\frac{T_{\text{eff}}}{8071.03} \right)^2 / 0.01045 \right) \right]. \quad (1)$$

Fig. 4 shows the H β (left panels), Mg I triplet (middle panels), and H α (right panels) spectral regions for the target stars (black) and the synthetic spectra (red) computed with the final results of the atmospheric parameters. The results for the atmospheric fundamental quantities and their

⁴ http://www.stsci.edu/hst/observatory/crds/castelli_kurucz_atlas.html

Table 3. List of basic and photometric parameters. The parallax (π) determined by [Gaia Collaboration \(2018\)](#), reddening parameter ($E(B-V)$) computed using 3D dustmaps by [Green et al. \(2019\)](#), the effective temperature (T_{eff}), surface gravity ($\log g$) and metallicity ($[M/H]$) estimated using $uvby\beta$ indices, T_{eff} computed from 2MASS, T_{eff} derived from UBV, and the estimated T_{eff} , $\log g$ and $[M/H]$ from the SED fitting are given.

KIC	π	$E(B-V)$	T_{eff} <i>uvbyβ</i>	$\log g$ <i>uvbyβ</i>	$[M/H]$ <i>uvbyβ</i>	T_{eff} 2MASS	T_{eff} UBV	T_{eff} SED	$\log g$ SED	$[M/H]$ SED
No.	(mas)	(mag)	(± 200 K)	(± 0.10 dex)	(± 0.13 dex)	(K)	(K)	(± 250 K)	(± 0.5 dex)	(dex)
3459226	3.3107 ± 0.0804	0.0303	-	-	-	7390 ± 280	6990 ± 250	7500	4.0	0.0 ± 0.35
4567097	2.0990 ± 0.0480	0.0581	-	-	-	9490 ± 510	10430 ± 350	9750	3.5	0.2 ± 0.25
4818496	4.0709 ± 0.0366	0.0593	-	-	-	9580 ± 290	9400 ± 270	9500	4.5	0.0 ± 0.35
5524045	2.1854 ± 0.0338	0.0449	-	-	-	8900 ± 360	9170 ± 260	9250	4.5	0.0 ± 0.35
5650229	1.6616 ± 0.0286	0.1377	-	-	-	9250 ± 340	9450 ± 330	9000	3.5	0.5 ± 0.30
6266219	2.5992 ± 0.0362	0.0310	-	-	-	7930 ± 260	7160 ± 260	7750	3.5	0.2 ± 0.25
7667560	2.8792 ± 0.0347	0.0245	-	-	-	8310 ± 290	8340 ± 220	8000	3.5	0.2 ± 0.25
9272082	2.5738 ± 0.0386	0.0254	8470	4.13	0.17	8010 ± 170	7920 ± 130	8000	3.5	0.5 ± 0.30
9349245	6.9544 ± 0.0343	0.0100	8130	4.27	0.22	7780 ± 170	7690 ± 120	7500	3.5	0.5 ± 0.30

errors are listed in Table 4. The spectroscopic T_{eff} values differ from those estimated using photometric indices ($uvby\beta$, 2MASS and UBV) and SED by an average temperature of about 360 K, 180 K, 350 K and 180 K, respectively. The spectroscopic $\log g$ and $[M/H]$ values are more consistent with those estimated from $uvby\beta$ photometry (average $\Delta \log g_{uvby\beta} = 0.18$ dex and $\Delta [M/H]_{uvby\beta} = 0.10$ dex) than those from SED (average $\Delta \log g_{\text{SED}} = 0.5$ dex and $\Delta [M/H]_{\text{SED}} = 0.23$ dex). Our final results (from spectroscopy) agree in general within the error limits with those from previous studies. The literature values for which this is not the case are shown in italics in Table 4. Particularly, we compared our T_{eff} and $\log g$ with those computed by [Mathur et al. \(2017\)](#); [Andrae et al. \(2018\)](#); [Murphy et al. \(2019\)](#) as shown, in panels (a) and (b) of Fig. 5, respectively. Based on the correlation coefficient (presented in the top right corner of each panel) with the weighted average of the literature values, T_{eff} is more consistent than $\log g$. The $v \sin i$ values are excellently consistent with the equatorial rotational velocity (v_{rot}) computed by [Trust et al. \(2020\)](#) as shown in Fig. 3, where all the stars are positioned either on or below the $\sin i = 1$ line.

4.4 Individual chemical abundances

The individual chemical abundances were determined based on direct fitting of the theoretical profiles of individual spectral lines. Since some targets are fast rotators and others are CP stars, lines are often blended and direct spectrum synthesis takes into account possible blends ([Romanovskaya et al. 2019](#)). We used the SYNTHV_NLTE code ([Tsymbal et al. 2019](#)) and a grid of atmosphere models pre-computed with the LLmodels code ([Shulyak et al. 2004](#)). This was implemented through an IDL visualization program, BINMAG6 ([Kochukhov 2018](#)). During spectral synthesis, local thermodynamic equilibrium (LTE) was assumed. For oxygen abundance analysis, we excluded the O I triplet (around 777.1–777.5 nm), since it is affected by non-LTE effects ([Przybilla et al. 2000](#)). For the same reason, we never considered Na I lines at 589.0 and 589.6 nm ([Takeda et al. 2009](#)) in our analysis. We adopted spectral line lists and atomic parameters

from the 3D release of the Vienna Atomic Line Database (VALD3; [Ryabchikova et al. 2015](#)).

We divided each spectrum into several intervals, each ≈ 5 nm wide, and derived the abundances in each interval by performing a χ^2 minimization of the difference between the observed and synthetic spectrum. The average individual chemical abundances are listed in Table 5. We used the errors on T_{eff} , $\log g$, $v \sin i$, ξ , position of the continuum, and accuracy of the oscillator strengths ($\log(\text{gf})$) of the considered lines to derive abundance uncertainties. For each element, the errors on abundance associated with the errors on each of the T_{eff} , $\log g$, $v \sin i$, ξ , position of the continuum, and the $\log(\text{gf})$ were added together in quadrature to get the total uncertainty. We note that the abundances of elements whose lines only appear in less than three segments should be taken with caution since they were computed from few lines.

Table 4. List of stellar parameters from spectroscopic analysis. The different columns show: identification number, effective temperatures (T_{eff}), surface gravity ($\log g$), metallicity ($[M/H]$), microturbulent velocity (ξ), projected rotational velocity ($v \sin i$) and radial velocity (v_{rad}). The literature values that do not agree within 1σ with the results from this study are given in italics.

KIC No.	T_{eff} (K)	$\log g$ (dex)	$[M/H]$ (dex)	ξ (km s^{-1})	$v \sin i$ (km s^{-1})	v_{rad} (km s^{-1})	References
3459226	7640 ± 150	3.94 ± 0.14	0.32 ± 0.08	3.78 ± 0.18	73 ± 5	-28.8 ± 2.2	1
	7410 ± 139	3.79 ± 0.14			< 120	-24.1 ± 24.6	2
	7519 ± 83	<i>3.62 ± 0.16</i>					3
	<i>7055 ± 140</i>						4
	7516 ± 80	4.23 ± 0.09					5
4567097	9820 ± 300	3.90 ± 0.12	0.08 ± 0.13	1.64 ± 0.35	83 ± 5	7.1 ± 2.4	1
	9935 ± 360	4.21 ± 0.20					3
	8712 ± 980						4
	9928 ± 347						5
4818496	9340 ± 180	3.91 ± 0.13	0.25 ± 0.10	2.26 ± 0.23	180 ± 8	11.8 ± 5.4	1
	8941 ± 323	3.69 ± 0.33					3
	9000 ± 185						4
	8936 ± 312	3.92 ± 0.08					5
						12.8 ± 0.8	6
5524045	9130 ± 210	3.77 ± 0.10	-0.15 ± 0.09	2.16 ± 0.17	218 ± 15	3.6 ± 13.0	1
	9267 ± 169	3.87 ± 0.11			201 ± 58	7.8 ± 36.2	2
	9217 ± 82	3.87 ± 0.16					3
	9189 ± 497						4
	9235 ± 80	<i>3.99 ± 0.06</i>					5
	<i>9500 ± 200</i>	4.0 ± 0.20		<i>1.0 ± 0.4</i>	215 ± 7		7
5650229	8950 ± 180	3.81 ± 0.12	0.19 ± 0.10	2.02 ± 0.19	251 ± 22	-9.2 ± 1.2	1
	9898 ± 420	3.88 ± 0.12			243 ± 33	-9.3 ± 22.1	2
	8879 ± 345	3.87 ± 0.24					3
	8533 ± 400						4
	8842 ± 309	3.89 ± 0.08					5
6266219	8030 ± 250	4.11 ± 0.17	0.63 ± 0.11	3.88 ± 0.23	62 ± 3	2.0 ± 1.5	1
	7996 ± 282	4.05 ± 0.16					3
	7765 ± 130						4
	8007 ± 280	4.09 ± 0.09					5
7667560	8330 ± 200	4.04 ± 0.16	0.16 ± 0.09	2.41 ± 0.29	147 ± 14	-20.2 ± 4.8	1
	8675 ± 320	4.08 ± 0.15					3
	8278 ± 390						4
	8669 ± 303	4.22 ± 0.09					5
9272082	8170 ± 190	4.02 ± 0.13	0.17 ± 0.10	3.63 ± 0.20	78 ± 3	5.7 ± 1.7	1
	<i>7551 ± 262</i>	3.91 ± 0.12			< 120	-20.8 ± 18.3	2
	<i>9077 ± 334</i>	4.15 ± 0.15					3
	8081 ± 340						4
	<i>9078 ± 317</i>	4.06 ± 0.08					5
9349245	7830 ± 260	4.06 ± 0.11	0.37 ± 0.12	3.33 ± 0.14	81 ± 3	-36.2 ± 6.3	1
	7683 ± 79	3.87 ± 0.11			< 120	-15.0 ± 23.6	2
	7914 ± 279	3.72 ± 0.29					3
	7870 ± 393						4
	7913 ± 276	4.17 ± 0.09					5
	<i>8300 ± 200</i>	4.00 ± 0.30		3.1 ± 0.5	80 ± 3		8
	<i>8000 ± 200</i>	<i>3.7 ± 0.1</i>		2.9 ± 0.1	82 ± 2		9

References: (1) This study; (2) Frasca et al. (2016); (3) Mathur et al. (2017); (4) Andrae et al. (2018); (5) Murphy et al. (2019); (6) Gontcharov (2006); (7) Niemczura et al. (2015); (8) Catanzaro et al. (2015); (9) Niemczura et al. (2017)

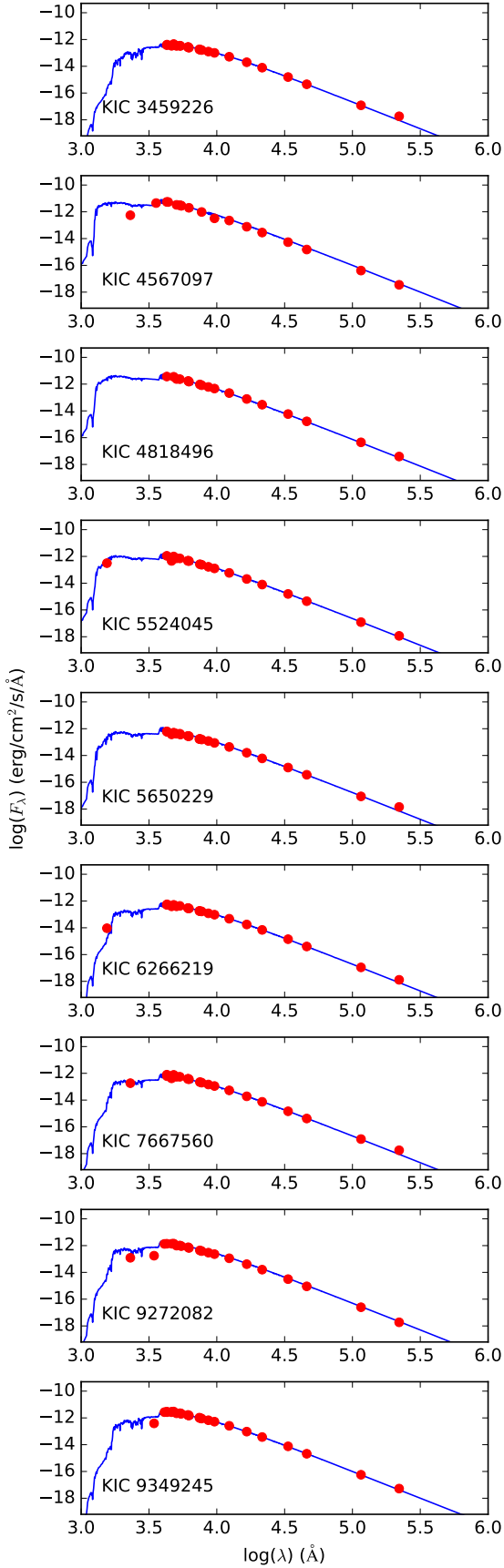


Figure 2. The red filled circles represent the SEDs of the target stars. The blue solid lines represent the spectra fitted to the data using the VOSA tool.

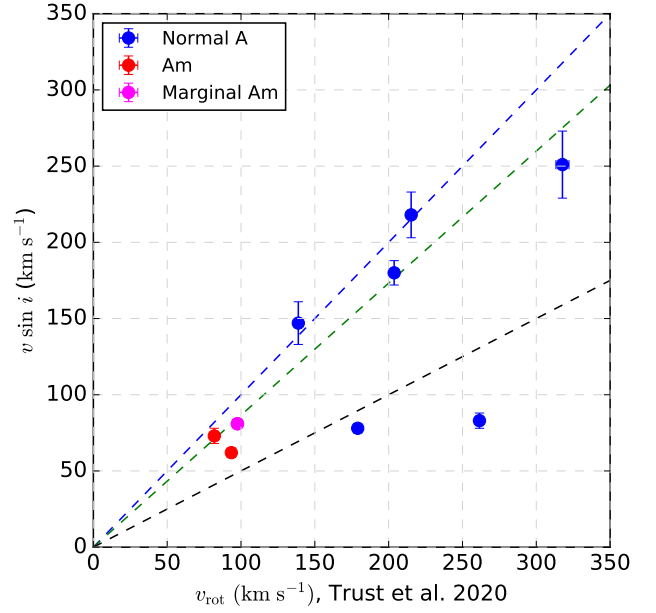


Figure 3. The projected rotational velocity $v \sin i$ as computed in this study compared with the equatorial rotational velocity v_{rot} by Trust et al. (2020). The blue, red, and magenta dots are normal A, Am, and marginal Am stars, respectively. The blue dashed line represents $\sin i = 1$ while the green and black ones correspond to $i = 60^\circ$, and 30° , respectively.

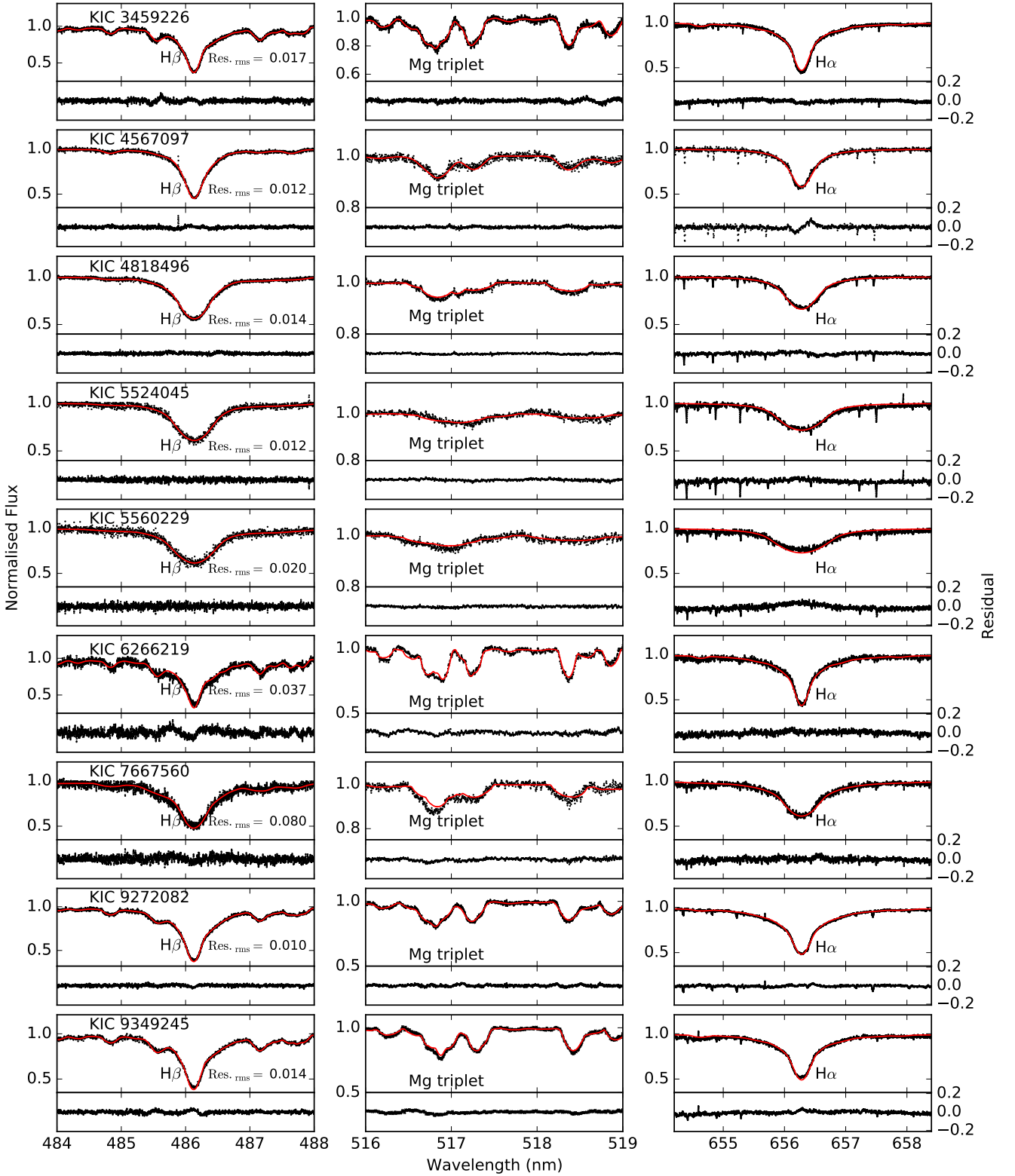


Figure 4. The H β (left), MgI triplet (middle) and H α (right) spectral regions for the target stars. The observed (black) and synthetic spectra (red) are shown. The root mean square value of the residuals (Res._{rms}) for each spectrum is given in the bottom-right corner of each H β panel.

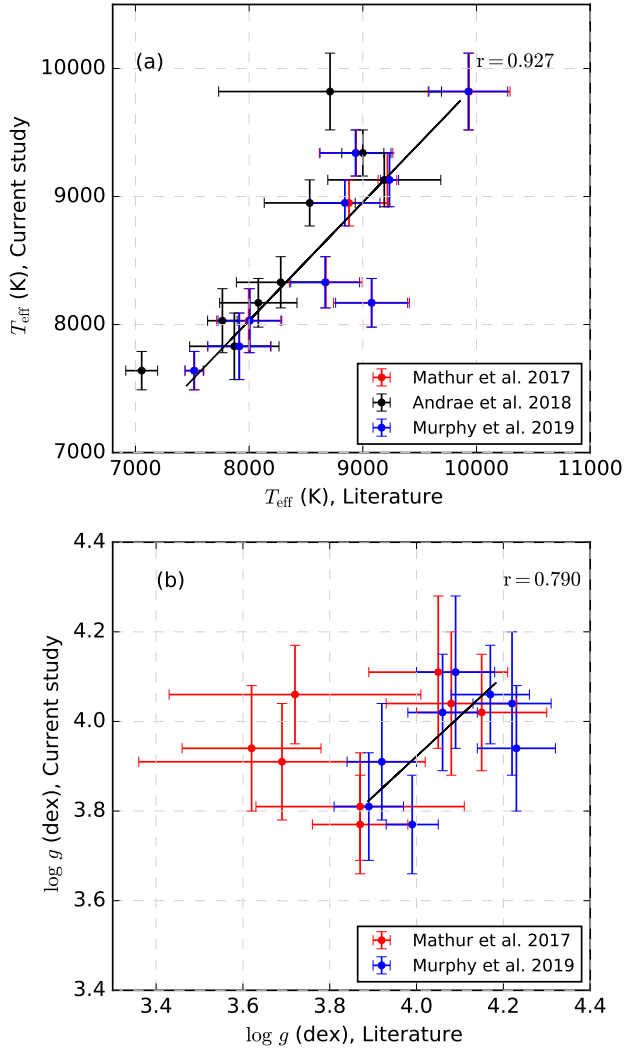


Figure 5. The T_{eff} and $\log g$ from the current study compared with those reported by Mathur et al. (2017) (red), Andrae et al. (2018) (black), and Murphy et al. (2019) (blue). The respective correlation coefficient, r , with the weighted average of the literature values is given in the top-right corner of each panel.

Table 5. Individual chemical abundances inferred for our target stars. The solar abundances are listed in the last column (Asplund et al. 2009). The values are expressed in the form $\log(N_{\text{el}}/N_{\text{Tot}})$. The number of segments from which each element was determined is given in brackets.

	KIC 3459226	KIC 4567097	KIC 4818496	KIC 5524045	KIC 5650229	KIC 6266219	KIC 7667560	KIC 9272082	KIC 9349245	Solar
C	-3.93 ± 0.16 (3)	-4.08 ± 0.11 (3)	-3.63 ± 0.10 (4)	-3.77 ± 0.09 (6)	-3.87 ± 0.10 (6)	-3.63 ± 0.12 (9)	-4.16 ± 0.09 (5)	-3.87 ± 0.13 (5)	-3.75 ± 0.09 (6)	-3.57
O	$-3.10 \pm 0.08^*$ (1)	$-3.22 \pm 0.15^*$ (1)	$-2.48 \pm 0.09^*$ (1)	$-2.61 \pm 0.10^*$ (2)	$-3.22 \pm 0.16^*$ (2)	$-3.06 \pm 0.10^*$ (2)	$-3.01 \pm 0.15^*$ (1)	$-2.95 \pm 0.09^*$ (1)	$-2.60 \pm 0.10^*$ (1)	-3.31
Na	$-4.12 \pm 0.07^*$ (1)	$-4.01 \pm 0.20^*$ (1)	$-5.02 \pm 0.10^*$ (1)	-	-	$-4.75 \pm 0.11^*$ (2)	$-4.92 \pm 0.13^*$ (2)	$-5.01 \pm 0.15^*$ (2)	$-4.89 \pm 0.09^*$ (2)	-5.76
Mg	-4.23 ± 0.20 (6)	-4.30 ± 0.14 (6)	-3.95 ± 0.11 (7)	-4.47 ± 0.10 (8)	-4.19 ± 0.22 (4)	-4.08 ± 0.11 (9)	-4.31 ± 0.13 (5)	-4.35 ± 0.11 (10)	-4.08 ± 0.09 (9)	-4.40
Al	$-4.61 \pm 0.09^*$ (1)	-	-	-	$-4.98 \pm 0.11^*$ (1)	-	-	$-5.25 \pm 0.13^*$ (1)	-	-5.55
Si	-3.91 ± 0.16 (8)	$-4.27 \pm 0.14^*$ (2)	$-4.00 \pm 0.11^*$ (1)	-4.01 ± 0.11 (3)	-3.71 ± 0.15 (3)	-3.82 ± 0.11 (10)	$-3.83 \pm 0.17^*$ (2)	-4.40 ± 0.09 (12)	-3.73 ± 0.10 (5)	-4.49
S	$-4.22 \pm 0.10^*$ (1)	-	-	-	-	-4.29 ± 0.09 (3)	-	$-4.48 \pm 0.15^*$ (1)	-	-4.88
K	$-5.92 \pm 0.09^*$ (1)	-	-	-	-	$-6.63 \pm 0.09^*$ (1)	-	$-6.97 \pm 0.09^*$ (1)	-	-6.97
Ca	-6.05 ± 0.14 (11)	-5.89 ± 0.12 (3)	-5.18 ± 0.14 (3)	-5.78 ± 0.18 (5)	-5.79 ± 0.12 (5)	-5.67 ± 0.10 (23)	-5.48 ± 0.20 (6)	-5.68 ± 0.09 (18)	-5.38 ± 0.10 (20)	-5.66
Sc	-9.35 ± 0.12 (4)	-8.92 ± 0.17 (5)	-9.04 ± 0.12 (4)	-9.06 ± 0.10 (4)	-8.82 ± 0.24 (4)	-9.11 ± 0.16 (7)	-8.66 ± 0.13 (5)	-8.70 ± 0.10 (10)	-8.96 ± 0.09 (3)	-8.85
Ti	-6.88 ± 0.17 (30)	-7.36 ± 0.10 (12)	-6.87 ± 0.12 (11)	-7.22 ± 0.10 (19)	-7.16 ± 0.16 (15)	-6.57 ± 0.09 (24)	-6.96 ± 0.13 (26)	-6.97 ± 0.12 (27)	-6.77 ± 0.10 (23)	-7.05
V	$-7.80 \pm 0.10^*$ (2)	$-7.87 \pm 0.13^*$ (1)	$-7.85 \pm 0.15^*$ (1)	-	$-7.86 \pm 0.12^*$ (2)	-6.98 ± 0.12 (4)	$-8.22 \pm 0.14^*$ (2)	-8.01 ± 0.10 (3)	-7.32 ± 0.12 (5)	-8.07
Cr	-6.04 ± 0.13 (5)	-6.58 ± 0.09 (7)	-6.39 ± 0.09 (7)	-6.95 ± 0.23 (7)	-6.30 ± 0.10 (7)	-5.53 ± 0.11 (17)	-6.36 ± 0.13 (10)	-6.30 ± 0.09 (19)	-6.15 ± 0.09 (18)	-6.36
Mn	-6.16 ± 0.19 (3)	$-6.37 \pm 0.11^*$ (1)	$-6.38 \pm 0.12^*$ (1)	-6.74 ± 0.12 (3)	-	-6.31 ± 0.10 (3)	-6.89 ± 0.12 (3)	-7.02 ± 0.23 (5)	-6.18 ± 0.08 (5)	-6.57
Fe	-3.89 ± 0.11 (79)	-4.63 ± 0.11 (17)	-4.24 ± 0.13 (38)	-4.68 ± 0.11 (33)	-4.27 ± 0.13 (31)	-3.82 ± 0.10 (83)	-4.25 ± 0.14 (43)	-4.61 ± 0.09 (43)	-4.18 ± 0.09 (44)	-4.50
Co	-5.94 ± 0.09 (6)	-	-	-	$-6.34 \pm 0.11^*$ (1)	-5.71 ± 0.13 (8)	-	-6.67 ± 0.16 (3)	-	-7.01
Ni	-5.10 ± 0.10 (16)	$-5.46 \pm 0.14^*$ (1)	$-6.22 \pm 0.19^*$ (1)	$-5.23 \pm 0.09^*$ (1)	-4.67 ± 0.16 (21)	-5.14 ± 0.09 (21)	-5.37 ± 0.15 (6)	-5.88 ± 0.09 (9)	-5.29 ± 0.09 (9)	-5.78
Cu	-7.05 ± 0.13 (3)	-	-	-	-	-6.37 ± 0.23 (3)	-	-7.17 ± 0.21 (3)	-	-7.81
Zn	-7.02 ± 0.09 (3)	-	-	-	-	$-7.27 \pm 0.13^*$ (1)	-	$-7.29 \pm 0.09^*$ (1)	$-7.17 \pm 0.09^*$ (1)	-7.44
Sr	-8.12 ± 0.11 (4)	$-9.36 \pm 0.12^*$ (2)	-	$-9.04 \pm 0.15^*$ (1)	$-8.84 \pm 0.10^*$ (1)	$-8.29 \pm 0.09^*$ (2)	$-8.84 \pm 0.22^*$ (2)	$-8.75 \pm 0.15^*$ (1)	-8.49 ± 0.14 (3)	-9.13
Y	-8.83 ± 0.19 (6)	-	$-9.81 \pm 0.11^*$ (1)	$-9.83 \pm 0.11^*$ (1)	-	-9.03 ± 0.19 (6)	-9.78 ± 0.09 (3)	-9.62 ± 0.11 (6)	-9.42 ± 0.09 (5)	-9.79
Zr	-8.51 ± 0.21 (4)	-	-	-	-9.51 ± 0.21 (3)	-8.98 ± 0.10 (3)	$-9.09 \pm 0.11^*$ (1)	$-9.18 \pm 0.14^*$ (2)	-9.12 ± 0.17 (13)	-9.44
Ba	-8.69 ± 0.19 (5)	-	-	-	$-10.06 \pm 0.11^*$ (2)	-8.44 ± 0.17 (5)	-9.77 ± 0.16 (3)	-9.45 ± 0.14 (5)	-8.76 ± 0.14 (3)	-9.83
La	-8.61 ± 0.13 (8)	-	-	-	-	-8.91 ± 0.21 (10)	-	-10.63 ± 0.10 (4)	-	-10.96
Ce	-8.93 ± 0.18 (7)	-	-	-	-	-8.61 ± 0.11 (9)	-	-10.02 ± 0.12 (5)	-	-10.44
Pr	$-9.79 \pm 0.10^*$ (1)	-	-	-	-	$-9.07 \pm 0.10^*$ (2)	-	-	-	-11.2
Nd	-8.73 ± 0.11 (5)	-	-	-	-	-8.79 ± 0.18 (7)	-	-	-	-10.6

These elements were only found in less than three segments.

5 COMMENTS ON INDIVIDUAL STARS

In this section we present the findings of the abundance analysis obtained for each target. The derived abundances and the estimated uncertainties are expressed as $\log(N_{el}/N_{Tot})$ and are reported in Table 5. Fig. 6 shows the abundance patterns for each star relative to the solar abundances (Asplund et al. 2009).

5.1 KIC 3459226 (BD +38 3705)

This star was classified as kA2hF0mF2 by Frasca et al. (2016) using LAMOST data (Cui et al. 2012; Zhao et al. 2012). We classified this target as kA2hF0mF3 using MKCLASS with HERMES data. Calcium and scandium are ≈ 0.4 and ≈ 0.5 dex below solar values, respectively, while the iron-peak and heavy elements such as Sr, Y, Zr, Ba, La, Ce, Pr, and Nd are clearly overabundant (values up to ≈ 2 dex). These over-abundances and spectral classification confirm the Am peculiarity of this star.

5.2 KIC 4567097 (HD 184469)

KIC 4567097 was reported in the Henry Draper (HD) catalog (Cannon & Pickering 1993) as a B9 star. Using MKCLASS, we obtained a spectral type of B9 III. No abundance analysis was found in the literature. The calcium abundance is ≈ 0.23 dex below solar value while scandium and the iron-peak elements are generally solar-like. Only few absorption lines were available and used to determine abundances. Based on the spectral class and chemical abundances obtained, we propose to consider KIC 4567097 as a non-Am star.

5.3 KIC 4818496 (HD 177592)

This object is listed in the HD catalog as an A0 star (Cannon & Pickering 1993) while our analysis classifies it as A1 V. The T_{eff} in this study is slightly higher than the values in the literature while our $\log g$ value is consistent (see Table 4). We found this star to be a fast rotator with a $v \sin i$ value of $180 \pm 8 \text{ km s}^{-1}$ which is consistent with the value computed by Trust et al. (2020). O, Na, Mg, Si, and Ca are overabundant (0.5–0.9 dex) while Sc and iron-peak elements are, on average, of solar content. Based on these results, we classify this star as a (chemically) normal A-type star.

5.4 KIC 5524045 (BD +40 3639)

KIC 5524045 was first classified as A0.5 Va+ (“a+” denotes higher luminosity MS star) by Niemczura et al. (2015) and subsequently as A1 V by Frasca et al. (2016). They are both in excellent agreement with our classification as a A1 V star. We observed this star to be fast rotating with $v \sin i = 219 \pm 12 \text{ km s}^{-1}$. Similar rotational velocities, $215 \pm 7 \text{ km s}^{-1}$ (Niemczura et al. 2015) and $201 \pm 58 \text{ km s}^{-1}$ (Frasca et al. 2016) were published before. All the measured elements are on average of solar type. The top panel of Fig. 7 shows that our abundances are in agreement with those determined by Niemczura et al. (2015). Based on the abundance pattern, we classify this star as normal.

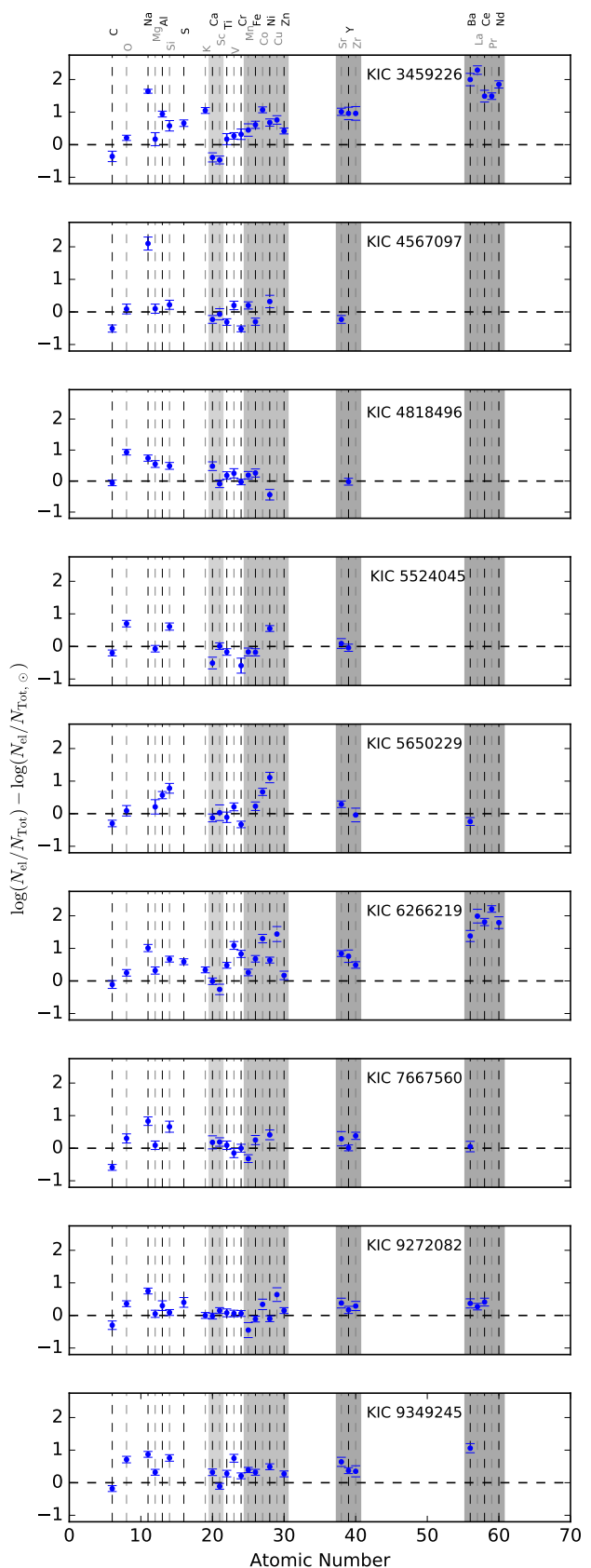


Figure 6. The individual chemical abundance patterns for our targets. The horizontal dashed line represents solar abundance (Asplund et al. 2009). The gray background highlights the light elements (Ca and Sc) and heavy elements (Sr, Y, Zr, Ba, La, Ce, Pr and Nd) important for Am classification. *MNRAS* **000**, 1–17 (2020)

5.5 KIC 5650229 (HD 226697)

This object was first listed as an A2 star in the HD catalog (Cannon & Pickering 1993). Recently, Frasca et al. (2016) classified it as a B9III or IV star. Our analysis indicates a spectral type as A1IV. The most recent study (Murphy et al. 2019) presents the star's T_{eff} and $\log g$ as 8842 ± 309 K and 3.89 ± 0.08 cm s^{-2} , respectively, which agrees with our result (8920 ± 190 K and 3.82 ± 0.11 cm s^{-2}). This star is a fast rotator whose $v \sin i$ was first reported as 243 ± 33 km s^{-1} (Frasca et al. 2016), which is consistent with our outcome of 252 ± 24 km s^{-1} . With exception of Al, Si, Co, and Ni which are overabundant (with an average abundance of ≈ 0.8 dex), the abundances of the other elements are solar-like and hence we consider this star as non-Am.

5.6 KIC 6266219 (TYC 3127-2016-1)

KIC 6266219 was listed among A-type stars in the nominal *Kepler* field (Balona 2013). We obtained its spectral type as kA3hA7mF1. The available $T_{\text{eff}} = 7996 \pm 282$ K and $\log g = 4.05 \pm 0.16$ cm s^{-2} (Mathur et al. 2017), $T_{\text{eff}} = 7765 \pm 130$ K (Andrae et al. 2018) and $T_{\text{eff}} = 8007 \pm 280$ K and $\log g = 4.09 \pm 0.09$ cm s^{-2} (Murphy et al. 2019) are consistent with our results. This object is a moderate rotator with $v \sin i$ of 60 km s^{-1} which agrees with the value given by Trust et al. (2020). The chemical abundances of Ca and Sc are solar-like while iron-peak and heavy elements are overabundant up to ≈ 2 dex. Based on the spectral type and chemical abundance pattern, we classify KIC 6266219 as an Am star.

5.7 KIC 7667560 (HD 177458)

KIC 7667560 was listed in the HD catalog as an A-type star by Cannon & Pickering (1993). Our spectral classification analysis revealed a spectral type of A3IV. The T_{eff} and $\log g$ values published by Mathur et al. (2017), Andrae et al. (2018), and Murphy et al. (2019) and are fully consistent with the values obtained in this study. Ca, Sc, iron-peak and heavy elements, on average, have solar-like abundances. Na (≈ 0.83 dex) and Si (≈ 0.66 dex) are overabundant. The chemical abundance pattern does not show Am characteristics.

5.8 KIC 9272082 (HD 179458)

This star was first classified as Am by Macrae (1952) and subsequently by Bertaud (1960). The most recent classification as A3V, by Frasca et al. (2016), matches our result, A4V. As shown in Table 4, only the T_{eff} computed by Andrae et al. (2018) using GAIA observations agrees with the T_{eff} obtained in this study. Our $\log g$ value agrees well with the values: 3.91 ± 0.12 dex (Frasca et al. 2016), 4.15 ± 0.15 dex (Mathur et al. 2017), and 4.06 ± 0.08 dex (Murphy et al. 2019). With exception of Na (≈ 0.75 dex) which is overabundant, abundances of the rest of the elements are solar-like. Based on the spectral classification and the chemical abundance pattern, we consider this star as non-Am.

5.9 KIC 9349245 (HD 185658)

KIC 9349245 is a MS A-type star as reported in various studies (e.g. Cannon & Pickering 1993, Gray et al. 2016, and Frasca et al. 2016) and it is included in the catalog of chemically peculiar stars (Renson & Manfroid 2009). We determined its spectral type as A8 IV (Sr) which is similar to the one given by Gray et al. (2016). The atmospheric parameters and velocities (ξ , $v \sin i$ and v_{rad}), within error limits, generally agree with values in the literature except for T_{eff} of Catanzaro et al. (2015) (see Table 4). The Ca and Sc abundances are solar-like, while iron-peak and heavy metals are moderately overabundant (with an average abundance of ≈ 0.5 dex). The chemical abundance pattern implies a marginal Am star. Similar observations were made by Catanzaro et al. (2015). The bottom panel of Fig. 7 shows a good agreement between the two studies.

6 LOCATION IN THE HR DIAGRAM

A precise positioning of both Am and non-Am stars in the HR diagram is useful for investigating possible systematic differences in the region occupied by these objects with regard to normal A stars. Moreover, all the targets studied in this paper are "hump and spike" stars and their position is useful to constrain the location of stars with r modes in the HR diagram.

The luminosity ($\log(L_{\star}/L_{\odot})$) of the target stars was calculated using the standard technique. We computed extinction from $A_V = 3.1 \times E(B-V)$, where $E(B-V)$ was obtained as discussed in Sect. 4.1. The bolometric correction (BC) was calculated using the temperature dependent function of Flower (1996) after a revision by Torres (2010), while the absolute magnitude (M_V) was determined using the GAIA parallaxes (Gaia Collaboration 2018). The uncertainties in $\log(L_{\star}/L_{\odot})$ result from uncertainties in V-band indices, parallax and T_{eff} . Having obtained precise T_{eff} and $\log(L_{\star}/L_{\odot})$ values, we also determined the stellar radius using the standard relation (from the Stefan–Boltzmann law) (Boltzmann 1884; Paul et al. 2015; Montambaux 2018),

$$\log\left(\frac{R}{R_{\odot}}\right) = 0.5 \log\left(\frac{L_{\star}}{L_{\odot}}\right) - 2.0 \log(T_{\text{eff}}) + 7.52340473. \quad (2)$$

The results and their uncertainties are listed in Table 6. Our values for R (except for KIC 4818496 and KIC 9272082) and $\log(L_{\star}/L_{\odot})$ are in good agreement with those determined by Murphy et al. (2019), as shown in panels (a) and (b) of Fig. 8, respectively.

Fig. 9 is the HR diagram showing the location of the normal A (blue) and Am (red) stars. With exception of KIC 4567097, which could be on the red giant phase, all our targets are located in the MS. This was also observed for KIC 4567097 from MK spectral classification in Sect. 3, where the luminosity class is III (giant), and from the spectral type obtained from SED fitting as discussed in Sect. 4.2. KIC 9272082 could be close to the end of its MS lifetime. All the Am stars lie within the observational δ Scuti instability strip determined by Murphy et al. (2019). With exception of KIC 7667560 and KIC 9272082, the normal A-type stars lie outside this instability strip.

Table 6. The different columns show: tag (for identification in the HR diagram in Fig. 9), identification (KIC) number, absolute magnitude (M_v), bolometric correction (BC), luminosity ($\log(L_\star/L_\odot)$) and stellar radius (R) as estimated from standard relations.

Tag	KIC No.	M_v (mag)	BC (mag)	$\log(L_\star/L_\odot)$ (dex)	R (R_\odot)
a	3459226	2.616 ± 0.145	0.0304 ± 0.0038	0.846 ± 0.056	1.50 ± 0.15
b	4567097	-0.820 ± 0.132	-0.2149 ± 0.0610	2.319 ± 0.028	4.98 ± 0.46
c	4818496	0.935 ± 0.092	-0.1735 ± 0.0410	1.600 ± 0.020	2.28 ± 0.15
d	5524045	0.918 ± 0.116	-0.0743 ± 0.0303	1.567 ± 0.034	2.46 ± 0.20
e	5650229	0.596 ± 0.128	-0.0512 ± 0.0276	1.687 ± 0.040	2.92 ± 0.26
f	6266219	1.848 ± 0.122	0.0239 ± 0.0024	1.156 ± 0.050	1.98 ± 0.24
g	7667560	1.850 ± 0.108	0.0140 ± 0.0130	1.159 ± 0.038	1.83 ± 0.17
h	9272082	0.924 ± 0.105	0.0225 ± 0.0047	1.526 ± 0.040	2.93 ± 0.27
i	9349245	2.290 ± 0.083	0.0279 ± 0.0084	0.978 ± 0.030	1.71 ± 0.17

7 CONCLUSION

In this paper we present a spectroscopic analysis of a sample of nine objects which are classified in literature as “hump and spike” stars. The sample comprises of both normal A and Am stars. The analysis is based on high-resolution spectra obtained with HERMES mounted at the Cassegrain focus of the 1.2-m Mercator telescope located at La Palma, Spain. For each star, we determined the spectral type and obtained fundamental parameters such as the effective temperature T_{eff} , surface gravity $\log g$, metallicity [M/H], microturbulent velocity ξ , projected rotational velocity $v \sin i$ and radial velocity v_{rad} . We also performed a detailed individual chemical abundance analysis for each target, obtained their luminosity $\log(L_\star/L_\odot)$ and derived an accurate position in the HR diagram.

All the stars are either fast (KIC 4818496, KIC 5524045, KIC 5650229, and KIC 7667560) or moderate (KIC 3459226, KIC 4567097, KIC 6266219, KIC 9272082, and KIC 9349245) rotators leading to severe blending of their spectral lines. To overcome this problem, we applied the spectral synthesis method in our analysis using different codes. Of all the stars in our sample, only two stars have high-resolution spectroscopic analysis reported in the literature, i.e. KIC 5524045 (Niemczura et al. 2015) and KIC 9349245 (Catanzaro et al. 2015). For the remaining 7 targets, it was the first time that a detailed spectroscopic analysis was done.

We classified KIC 4567097 as a giant while the rest are dwarfs. So far, KIC 6266219 and KIC 9272082 have been considered as chemically normal and Am, respectively (e.g. Trust et al. 2020). Based on our spectral classification analysis and the resulting chemical abundance pattern, we reclassify KIC 6266219 as an Am star (kA3hA7mF1) while KIC 9272082 as chemically normal. Therefore, we conclude that our sample contains two Am stars (KIC 3459226 and KIC 6266219) and one marginal Am star (KIC 9349245), and six targets that are considered as non-Am stars (KIC 4567097, KIC 4818496, KIC 5524045, KIC 5650229, KIC 7667560, and KIC 9272082). With exception of the moderate rotators KIC 4567097 and KIC 9272082, the remaining 4 non-Am stars are fast rotators ($v \sin i > 120 \text{ km s}^{-1}$), a property that facilitates mixing against atomic diffusion while minimising the chemical peculiarity. In addition, Fig. 3 nicely shows that the Am and marginal Am stars are the slow rotators in the sample, which sup-

ports the idea that slow rotation facilitates the creation of chemical peculiarities.

The availability of HERMES and other spectrographs capable of high-resolution spectroscopy will allow us, in future, to continue the study of the “hump and spike” stars. Particularly, we will segregate Am from non-Am stars in the “hump and spike” star sample. In the near future, modelling of these stars will shed light on the interaction of chemical peculiarity, rotation, and Rossby waves.

ACKNOWLEDGMENTS

The Swedish International Development Co-operation Agency (SIDA) through the International Science Program (ISP) of Uppsala University financed this study. The part of work presented here is supported by the Belgo-Indian Network for Astronomy & Astrophysics (BINA), approved by the International Division, Department of Science and Technology (DST, Govt. of India; DST/INT/Belg/P-02) and the Belgian Federal Science Policy Office (BELSPO, Govt. of Belgium; BL/33/IN12). Based on observations made with the Mercator Telescope, operated on the island of La Palma by the Flemish Community, at the Spanish Observatorio del Roque de los Muchachos of the Instituto de Astrofísica de Canarias. This work makes use of VOSA, developed under the Spanish Virtual Observatory project supported by the Spanish MINECO through grant AyA2017-84089. VOSA has been partially updated by using funding from the European Union’s Horizon 2020 Research and Innovation Programme, under Grant Agreement 776403 (EXOPLANETS-A). We thank Dr. Yves Frémat for kindly providing the GIRFIT code. We acknowledge Professor Vadim Tsymbal for helpful comments and discussions. We acknowledge the anonymous reviewer for his/her careful reading of our manuscript and many insightful comments and suggestions which improved this paper.

DATA AVAILABILITY

The data underlying this article are available in the Figshare repository at <https://dx.doi.org/10.6084/m9.figshare.13604348.v2>.

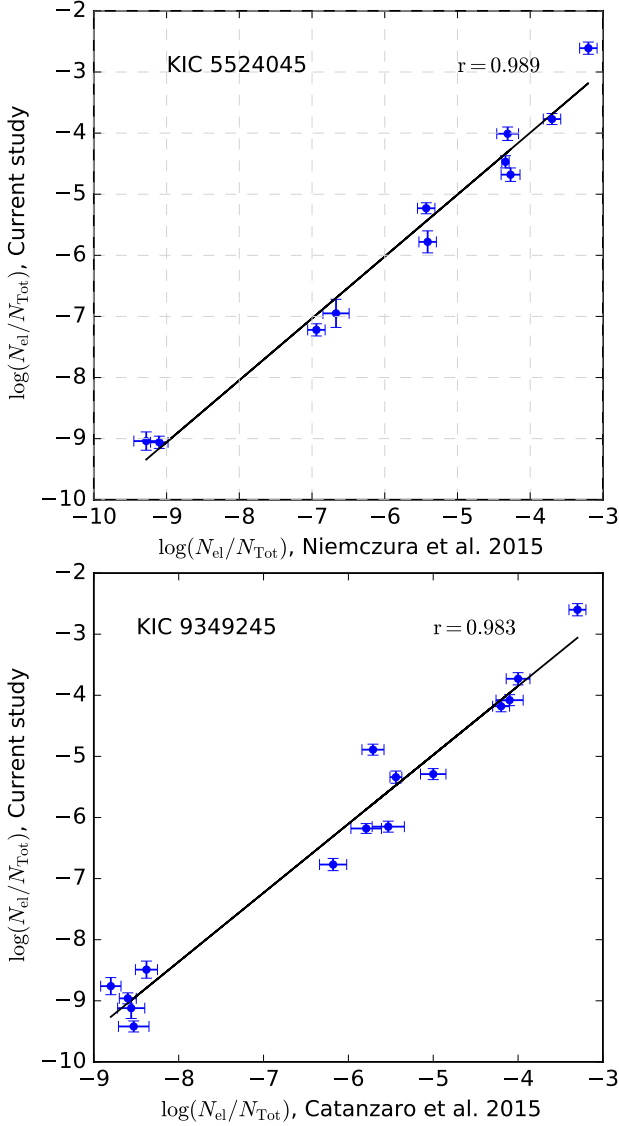


Figure 7. A comparison of our individual chemical abundances for KIC 5524045 (top panel) with values by Niemczura et al. (2015) and KIC 9349245 (bottom panel) with those determined by Catanzaro et al. (2015). The corresponding correlation coefficient, r , is given in the top-right corner of each panel.

REFERENCES

- Abt H. A., 2009, *AJ*, 138, 28
 Alecian G., 1996, *A&A*, 310, 872
 Andrae R., et al., 2018, *A&A*, 616, A8
 Ashoka B. N., et al., 2000, *Bulletin of the Astronomical Society of India*, 28, 251
 Asplund M., Grevesse N., Sauval A. J., Scott P., 2009, *ARA&A*, 47, 481
 Aurière M., et al., 2007, *A&A*, 475, 1053
 Baglin A., Michel E., Auvergne M., COROT Team 2006, in *Proceedings of SOHO 18/GONG 2006/HELAS I, Beyond the spherical Sun*. p. 34
 Balona L. A., 2013, *MNRAS*, 431, 2240
 Balona L. A., Catanzaro G., Abedigamba O. P., Ripepi V., Smalley B., 2015, *MNRAS*, 448, 1378

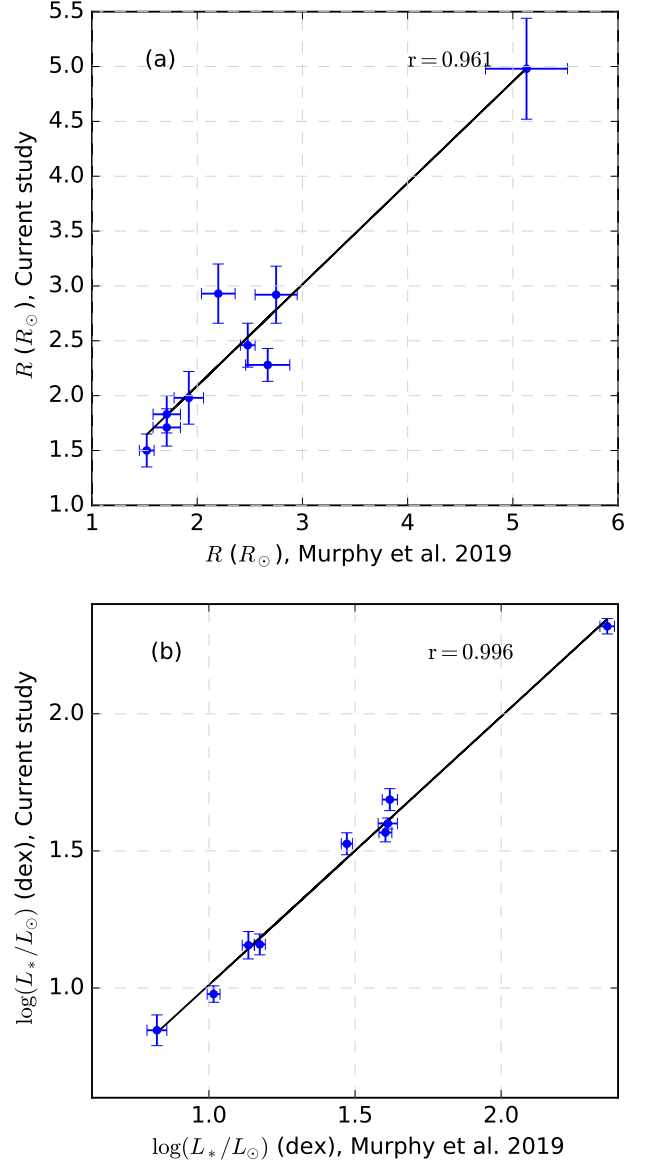


Figure 8. Stellar radius and $\log(L_{*}/L_{\odot})$ from the current study compared with those determined by Murphy et al. (2019). The respective correlation coefficient, r , is given in the top-right corner of each panel.

- Bayo A., Rodrigo C., Barrado Y Navascués D., Solano E., Gutiérrez R., Morales-Calderón M., Allard F., 2008, *A&A*, 492, 277
 Bertaud C., 1960, *Journal des Observateurs*, 43, 129
 Bianchi L., GALEX Team 2000, *Mem. Soc. Astron. Italiana*, 71, 1123
 Blanco-Cuaresma S., 2019, *MNRAS*, 486, 2075
 Blanco-Cuaresma S., Soubiran C., Heiter U., Jofré P., 2014, *A&A*, 569, A111
 Bohlender D. A., Dworetzky M. M., Jomaron C. M., 1998, *ApJ*, 504, 533
 Boltzmann L., 1884, *Annalen der Physik*, 258, 291
 Borucki W. J., et al., 2010, *Science*, 327, 977
 Braithwaite J., Spruit H. C., 2004, *Nature*, 431, 819
 Brown T. M., Latham D. W., Everett M. E., Esquerdo G. A., 2011, *AJ*, 142, 112
 Browning M. K., Brun A. S., Toomre J., 2004, *ApJ*, 601, 512

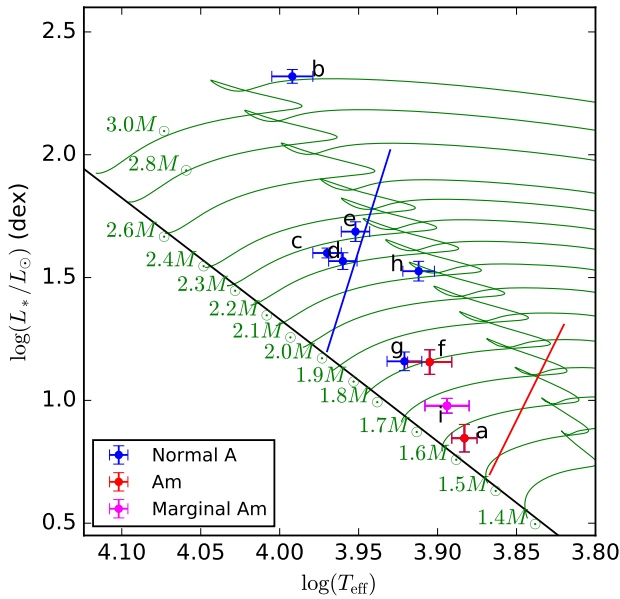


Figure 9. The HR diagram showing evolutionary phase of target stars. The blue, red, and magenta dots are normal A, Am, and marginal Am stars, respectively. The black solid line represents the zero-age main sequence (ZAMS) while the green solid lines are evolutionary tracks for different masses. The blue and red solid lines indicate the blue and red edges of the observational δ Scuti instability strip reported by [Murphy et al. \(2019\)](#).

Cannon A. J., Pickering E. C., 1993, *VizieR Online Data Catalog*, p. III/135A
 Castelli F., Kurucz R. L., 2003, in Piskunov N., Weiss W. W., Gray D. F., eds, *IAU Symposium Vol. 210, Modelling of Stellar Atmospheres*. p. A20
 Castelli F., Gratton R. G., Kurucz R. L., 1997, *A&A*, **318**, 841
 Catanzaro G., et al., 2015, *MNRAS*, **451**, 184
 Chambers K. C., et al., 2016, preprint, ([arXiv:1612.05560](#))
 Claverie A., Isaak G. R., McLeod C. P., van der Raay H. B., Roca Cortes T., 1981, *Nature*, **293**, 443
 Conti P. S., 1970, *PASP*, **82**, 781
 Costa G., Girardi L., Bressan A., Marigo P., Rodrigues T. S., Chen Y., Lanza A., Goudfrooij P., 2019, *MNRAS*, **485**, 4641
 Cui X.-Q., et al., 2012, *Research in Astronomy and Astrophysics*, **12**, 1197
 Cutri R. M., et al., 2003, *VizieR Online Data Catalog*, p. II/246
 Dziembowski W., Krolkowska M., Kosovichev A., 1988, *Acta Astron.*, **38**, 61
 Eisner N. L., et al., 2020, *MNRAS*, **494**, 750
 Floquet M., 1970, *A&AS*, **1**, 1
 Flower P. J., 1996, *ApJ*, **469**, 355
 Fossati L., Bagnulo S., Landstreet J., Wade G., Kochukhov O., Monier R., Weiss W., Gebran M., 2008, *A&A*, **483**, 891
 Frasca A., et al., 2016, *A&A*, **594**, A39
 Frémat Y., Neiner C., Hubert A. M., Floquet M., Zorec J., Janot-Pacheco E., Renan de Medeiros J., 2006, *A&A*, **451**, 1053
 Gaia Collaboration 2018, *VizieR Online Data Catalog*, p. I/345
 Gandolfi D., et al., 2018, *A&A*, **619**, L10
 Gebran M., Monier R., 2008, *A&A*, **483**, 567
 Gebran M., Monier R., Richard O., 2008, *A&A*, **479**, 189
 Gebran M., Vick M., Monier R., Fossati L., 2010, *A&A*, **523**, A71
 Gebran M., Monier R., Royer F., Lobel A., Blomme R., 2014, in Mathys G., Griffin E. R., Kochukhov O., Monier R., Wahlgren G. M., eds, *Putting A Stars into Context: Evolution, Environ-*

ment, and Related Stars. pp 193–198 ([arXiv:1312.0442](#))
 Gehrels N., Spergel D., WFIRST SDT Project 2015, *J. Phys.: Conf. Ser.*, **610**, 012007
 Gontcharov G. A., 2006, *Astron. Lett.*, **32**, 759
 Gray R. O., Corbally Christopher J., 2009, *Stellar Spectral Classification*. Princeton University Press
 Gray R. O., Corbally C. J., 2014, *AJ*, **147**, 80
 Gray R. O., Corbally C. J., Garrison R. F., McFadden M. T., Robinson P. E., 2003, *AJ*, **126**, 2048
 Gray R. O., et al., 2016, *AJ*, **151**, 13
 Green G. M., 2018, *JOSS*, **3**, 695
 Green G. M., Schlafly E., Zucker C., Speagle J. S., Finkbeiner D., 2019, *ApJ*, **887**, 93
 Hauck B., Mermilliod M., 1998, *A&AS*, **129**, 431
 Herdin A., Paurzen E., Netopil M., 2016, *A&A*, **585**, A67
 Høg E., et al., 2000a, *A&A*, **355**, L27
 Høg E., et al., 2000b, *A&A*, **357**, 367
 Howard A. W., et al., 2013, *Nature*, **503**, 381
 Howell S. B., et al., 2014, *PASP*, **126**, 398
 Hui-Bon-Hoa A., 2000, *A&AS*, **144**, 203
 Johnson H. L., Morgan W. W., 1953, *ApJ*, **117**, 313
 Jones T. J., Wolff S. C., 1974, *PASP*, **86**, 67
 Joshi S., et al., 2003, *MNRAS*, **344**, 431
 Joshi S., Mary D. L., Martinez P., Kurtz D. W., Girish V., Seetha S., Sagar R., Ashoka B. N., 2006, *A&A*, **455**, 303
 Joshi S., Mary D. L., Chakradhari N. K., Tiwari S. K., Billaud C., 2009, *A&A*, **507**, 1763
 Joshi S., Ryabchikova T., Kochukhov O., Sachkov M., Tiwari S. K., Chakradhari N. K., Piskunov N., 2010, *MNRAS*, **401**, 1299
 Joshi S., et al., 2012, *MNRAS*, **424**, 2002
 Joshi S., et al., 2016, *A&A*, **590**, A116
 Joshi S., Semenko E., Moiseeva A., Sharma K., Joshi Y. C., Sachkov M., Singh H. P., Yerra B. K., 2017, *MNRAS*, **467**, 633
 Kahraman Aliçavuş F., et al., 2016, *MNRAS*, **458**, 2307
 Kaler J. B., 1989, *Stars and their spectra. an introduction to spectral sequence*. Cambridge University Press
 Kassounian S., Gebran M., Paletou F., Watson V., 2019, *OAst*, **28**, 68
 Kesseli A. Y., West A. A., Veyette M., Harrison B., Feldman D., Bochanski J. J., 2017, *ApJS*, **230**, 16
 Khokhlova V. L., 1981, in *Chemically peculiar stars of the upper main sequence*. Université de Liège, pp 457–463
 Kochukhov O., 2018, *BinMag: Widget for comparing stellar observed with theoretical spectra (ascl:1805.015)*
 Kron G. E., 1947, *PASP*, **59**, 261
 Kupka F., Piskunov N., Ryabchikova T. A., Stempels H. C., Weiss W. W., 1999, *A&AS*, **138**, 119
 Kurtz D. W., Martinez P., 2000, *BaltA*, **9**, 253
 LaSala J., 1994, in Corbally C. J., Gray R. O., Garrison R. F., eds, *Astronomical Society of the Pacific Conference Series Vol. 60, The MK Process at 50 Years: A Powerful Tool for Astrophysical Insight*. p. 312
 Macrae D. A., 1952, *ApJ*, **116**, 592
 Maíz Apellániz J., Weiler M., 2018, *A&A*, **619**, A180
 Martinez P., et al., 2001, *A&A*, **371**, 1048
 Masana E., Jordi C., Ribas I., 2006, *A&A*, **450**, 735
 Mathur S., et al., 2017, *ApJS*, **229**, 30
 McDonald I., Zijlstra A. A., Boyer M. L., 2012, *MNRAS*, **427**, 343
 Mermilliod J.-C., Mermilliod M., Hauck B., 1997, *A&AS*, **124**, 349
 Michaud G., 1970, *ApJ*, **160**, 641
 Michaud G., Charland Y., 1986, *ApJ*, **311**, 326
 Michaud G., Tarasick D., Charland Y., Pelletier C., 1983, *ApJ*, **269**, 239
 Michaud G., Richard O., Richer J., VandenBerg D. A., 2004, *ApJ*, **606**, 452

- Montambaux G., 2018, *Foundations of Physics*, 48, 395–410
- Moon T., 1985, *Comm. Univ. London Obs.*, 78, 1
- Moon T. T., Dworetzky M. M., 1985, *MNRAS*, 217, 305
- Morgan W. W., Keenan P. C., Kellman E., 1943, An atlas of stellar spectra, with an outline of spectral classification. University of Chicago press
- Mosser B., Baudin F., Lanza A. F., Hulot J. C., Catala C., Baglin A., Auvergne M., 2009, *A&A*, 506, 245
- Murphy S. J., 2014, PhD thesis, Jeremiah Horrocks Institute, University of Central Lancashire, Preston, UK <EMAIL>murphy@physics.usyd.edu.au</EMAIL>
- Murphy S. J., Hey D., Van Reeth T., Bedding T. R., 2019, *MNRAS*, 485, 2380
- Napiwotzki R., Schoenberner D., Wenske V., 1993, *A&A*, 268, 653
- Niemczura E., et al., 2015, *MNRAS*, 450, 2764
- Niemczura E., et al., 2017, *MNRAS*, 470, 2870
- Noyes R. W., Hartmann L. W., Baliunas S. L., Duncan D. K., Vaughan A. H., 1984, *ApJ*, 279, 763
- Oja T., 1985, *A&AS*, 59, 461
- Paul H., Greenberger D. M., Stenholm S. T., Schleich W. P., 2015, *Physica Scripta Volume T*, 165, 014027
- Preston G. W., 1974, *ARA&A*, 12, 257
- Przybilla N., Butler K., Becker S. R., Kudritzki R. P., Venn K. A., 2000, *A&A*, 359, 1085
- Ramírez I., Meléndez J., 2005, *ApJ*, 626, 465
- Raskin G., et al., 2011, *A&A*, 526, A69
- Rauer H., et al., 2014, *Exp. Astron.*, 38, 249
- Renson P., Manfroid J., 2009, *A&A*, 498, 961
- Richard O., Michaud G., Richer J., 2001, *ApJ*, 558, 377
- Richer J., Michaud G., Turcotte S., 2000, *ApJ*, 529, 338
- Ricker G. R., et al., 2014, *JATIS*, 1, 14003
- Romanovskaya A., Ryabchikova T., Shulyak D., Perraut K., Valyavin G., Burlakova T., Galazutdinov G., 2019, *MNRAS*, 488, 2343
- Romanyuk I. I., 2007, *Astrophys. Bull.*, 62, 62
- Rucinski S., Carroll K., Kuschnig R., Matthews J., Stibrany P., 2003, *Adv. Space Res.*, 31, 371
- Ryabchikova T., Piskunov N., Kurucz R. L., Stempels H. C., Heiter U., Pakhomov Y., Barklem P. S., 2015, *Phys. Scr.*, 90, 054005
- Saio H., 1981, *ApJ*, 244, 299
- Saio H., Kurtz D. W., Murphy S. J., Antoci V. L., Lee U., 2018, *MNRAS*, 474, 2774
- Santos N. C., Israelian G., Mayor M., Bento J. P., Almeida P. C., Sousa S. G., Ecuillon A., 2005, *A&A*, 437, 1127
- Sekiguchi M., Fukugita M., 2000, *AJ*, 120, 1072
- Shulyak D., Tsybmal V., Ryabchikova T., Stütz C., Weiss W. W., 2004, *A&A*, 428, 993
- Skrutskie M. F., et al., 2006, *AJ*, 131, 1163
- Smalley B., 1993, *A&A*, 274, 391
- Smith K. C., 1997, *A&A*, 319, 928
- Snedden C., Bean J., Ivans I., Lucatello S., Sobek J., 2012, MOOG: LTE line analysis and spectrum synthesis, Astrophysics Source Code Library (ascl:1202.009)
- Soufi F., Goupil M. J., Dziembowski W. A., 1998, *A&A*, 334, 911
- Sousa S. G., et al., 2015, *A&A*, 576, A94
- Stateva I. K., Iliev I. K., Budaj J., Barzova I. S., 2009, *BAJ*, 12, 29
- Takeda Y., Han I., Kang D.-I., Lee B.-C., Kim K.-M., 2008, *J. Korean Astron.*, 41, 83
- Takeda Y., Kang D.-I., Han I., Lee B.-C., Kim K.-M., 2009, *PASJ*, 61, 1165
- Talon S., Richard O., Michaud G., 2006, *ApJ*, 645, 634
- Théado S., Vauclair S., Alecian G., LeBlanc F., 2011, in Alecian G., Belkacem K., Samadi R., Valls-Gabaud D., eds, SF2A-2011: Proceedings of the Annual meeting of the French Society of Astronomy and Astrophysics. pp 253–256
- Tkachenko A., Van Reeth T., Tsybmal V., Aerts C., Kochukhov O., Deboscher J., 2013, *A&A*, 560, A37
- Torres G., 2010, *AJ*, 140, 1158
- Trust O., Jurua E., De Cat P., Joshi S., 2020, *MNRAS*, 492, 3143
- Tsybmal V., Ryabchikova T., Sitnova T., 2019, in Kudryavtsev D. O., Romanyuk I. I., Yakunin I. A., eds, *Astronomical Society of the Pacific Conference Series Vol. 518, Physics of Magnetic Stars*. pp 247–252
- Turcotte S., 2002, in Aerts C., Bedding T. R., Christensen-Dalsgaard J., eds, *Astronomical Society of the Pacific Conference Series Vol. 259, IAU Colloq. 185: Radial and Non-radial Pulsations as Probes of Stellar Physics*. p. 258 ([arXiv:astro-ph/0111179](https://arxiv.org/abs/astro-ph/0111179))
- Turcotte S., 2003, in Balona L. A., Henrichs H. F., Medupe R., eds, *Astronomical Society of the Pacific Conference Series Vol. 305, Magnetic Fields in O, B and A Stars: Origin and Connection to Pulsation, Rotation and Mass Loss*. p. 199 ([arXiv:astro-ph/0304424](https://arxiv.org/abs/astro-ph/0304424))
- Vick M., Michaud G., Richer J., Richard O., 2010, *A&A*, 521, A62
- Vick M., Michaud G., Richer J., Richard O., 2011, *A&A*, 526, A37
- Watson W. D., 1970, *ApJL*, 162, L45
- Wenger M., et al., 2000, *A&AS*, 143, 9
- Wright E. L., et al., 2010, *AJ*, 140, 1868
- Zhao G., Zhao Y.-H., Chu Y.-Q., Jing Y.-P., Deng L.-C., 2012, *Research in Astronomy and Astrophysics*, 12, 723

This paper has been typeset from a $\text{\TeX}/\text{\LaTeX}$ file prepared by the author.